Biophysical Journal
Article

Biophysical Society

Dynamic Model Exposes the Energetics and Dynamics of the Injection Machinery for Bacteriophage T4

Ameneh Maghsoodi,[1,*] Anupam Chatterjee,[2] Ioan Andricioaei,[2] and Noel C. Perkins[1]
[1]Department of Mechanical Engineering, University of Michigan, Ann Arbor, Michigan and [2]Department of Chemistry, University of California, Irvine, Irvine, California

ABSTRACT Bacteriophage T4 infects the bacterial host (*Escherichia coli*) using an efficient genomic delivery machine that is driven by elastic energy stored in a contractile tail sheath. Although the atomic structure of T4 is largely known, the dynamics of its fascinating injection machinery is not understood. This article contributes, to our knowledge, the first predictions of the energetics and dynamics of the T4 injection machinery using a novel dynamic model. The model employs an atomistic (molecular dynamics) representation of a fraction of the sheath structure to generate a continuum model of the entire sheath that also couples to a model of the viral capsid and tail tube. The resulting model of the entire injection machine reveals estimates for the energetics, timescale, and pathway of the T4 injection process as well as the force available for cell rupture. It also reveals the large and highly nonlinear conformational changes of the sheath whose elastic energy drives the injection process.

INTRODUCTION

The structure and function of bacteriophages continue to attract considerable research attention (1–12) because of implications for future nanotechnology devices for DNA (deoxyribonucleic acid) transfection and for experimental phage therapies (see, for example, (13–15)). Bacteriophage T4 is one of the most common and complex of the tailed viruses from the family *Myoviridae* that infects *Escherichia coli* using a highly efficient contractile tail. As illustrated in Fig. 1 *A*, the structure of T4 consists of a large icosahedral multiprotein capsid containing the 172-kilobase pairs double-stranded DNA genome (7) and a long contractile tail that transmits genomic DNA from the capsid to a bacterial host. The 1195 Å-long and 860 Å-wide capsid (8) (Fig. 1 *B*) connects to the tail assembly through a neck (composed of gene products (gp) 13, 14, and 15) (1). The tail assembly consists of a 96 Å-diameter and 940 Å-long noncontractile tube (gp19) (2) that forms a conduit for DNA transmission from the capsid into the host cell. The tail tube is surrounded by a contractile sheath formed from six helical protein strands of gp18 (7). The springlike sheath is composed of 138 copies of gp18 subunits arranged into the six helical protein strands that also form 23 hexameric rings ((1); and Fig. 1, *C* and *D*). The sheath is attached to the neck at the upper end and to the baseplate at the lower end (9) in Fig. 1, *C* and *D*. The long and short tail fibers attached to the baseplate are responsible for recognizing the bacterial host and binding to the host membrane (Fig. 1 *A*).

Phage T4 infects *E. coli* through a four-stage process, schematically illustrated in Fig. 2, which includes 1) recognizing, 2) binding, and 3) piercing the host cell membrane, followed by 4) translocating genomic DNA into the host cytoplasm. Before piercing the host cell membrane, the long fiber tips interact reversibly with the cell receptor proteins to recognize the host (Fig. 2 *A*) and then the short fibers anchor irreversibly to the cell (Fig. 2 *B*). When the baseplate undergoes a large conformational change from a high-energy hexagonal dome-shape structure (Fig. 1 *C*) to a low-energy flatter star-shape structure (1,5) (Fig. 1 *D*), the end of the tail tube is released from the baseplate and the sheath undergoes a rapid and large irreversible contraction (1) which drives the tail tube into the cell membrane (Fig. 2 *C*). The interaction of the tail tube tip with the specific receptors of the host cytoplasmic membrane triggers DNA ejection from the capsid into the host cytoplasm (1) (Fig. 2 *D*).

During contraction, the sheath gp18 subunits largely translate and rotate as rigid bodies without significant changes in structure. After rotation and translation, the twist and rise between adjacent rings of subunits change from

Submitted January 24, 2017, and accepted for publication May 4, 2017.
*Correspondence: maghsudi@umich.edu
Editor: Wilma Olson.
http://dx.doi.org/10.1016/j.bpj.2017.05.029

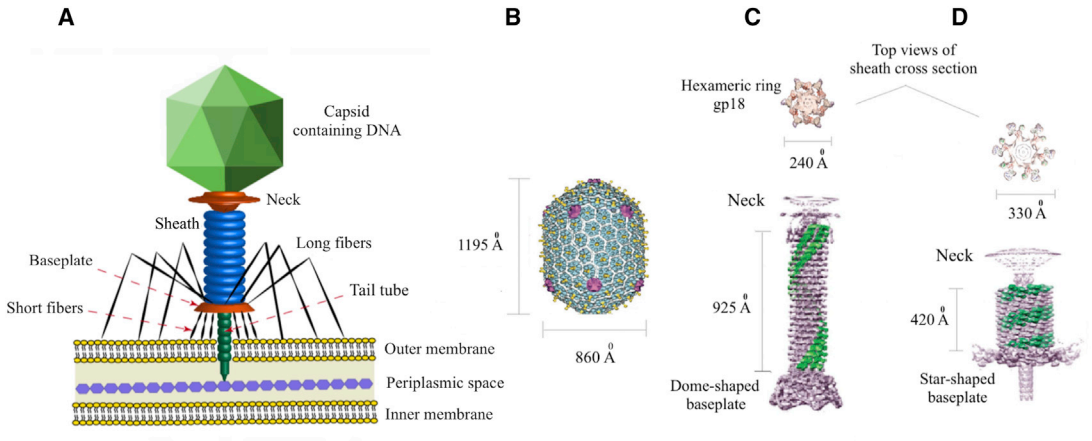

FIGURE 1 (*A*) Structural components of bacteriophage T4. Images (*B–D*) show cryo-EM-resolved components of T4 including: (*B*) the multiprotein icosahedral capsid (adapted with permission from (8), Copyright (2004) National Academy of Sciences, Washington, DC), (*C*) neck/tail assembly/baseplate in precontraction (extended) conformation, and (*D*) neck/tail assembly/baseplate in postcontraction (contracted) conformation (adapted with permission from (6)). To see this figure in color, go online.

17.2 to 32.9° and from 40.6 to 16.4 Å, respectively. Accordingly, the sheath undergoes a large conformational change from an extended (high-energy) state that is 925 Å-long and 240 Å-diameter to a contracted (low-energy) state that is 420 Å-long and 330 Å-diameter (7); refer to Fig. 1, *C* and *D*. During sheath contraction, the tail assembly and capsid simultaneously rotate about (by 345.4°) and translate along (by 505 Å) the tail tube axis (7). The rapid rotation and translation of the tail assembly creates a combination of torque and thrust on the host, which effectively pierces the host membrane.

Although the above atomic structure and protein composition of T4 has been studied extensively by cryo-electron microscopy (cryo-EM) and x-ray crystallography (see, for example, (1,6,7)), there is little known about the dynamics of sheath contraction driving the injection process. Arisaka et al. (16) estimated the free energy of sheath contraction to be ∼3400 kcal/mol gp18 for urea-induced contraction and ∼6000 kcal/mol gp18 for heat-induced contraction. Falk and James (17) employed elasticity theory to estimate the free energy of the sheath during contraction as well as a lower-bound estimate (103 pN) of the cell rupture force. Extending beyond these studies, this article contributes the first predictions of the dynamic behavior of the T4 injection machinery using, to our knowledge, a novel modeling approach. The approach begins with an atomistic molecular dynamics (MD) model of a fraction of the sheath that is sufficient to estimate its elastic properties. Those properties are employed in a companion continuum model of the entire sheath that also couples to a model of the capsid and tail tube assembly. The resulting model of the entire T4 injection machine predicts the nonlinear and rapid dynamic conformational changes induced during the injection process. Doing so exposes the energetics, timescale, and pathway of these dynamical changes as well as the available force for piercing the cell membrane.

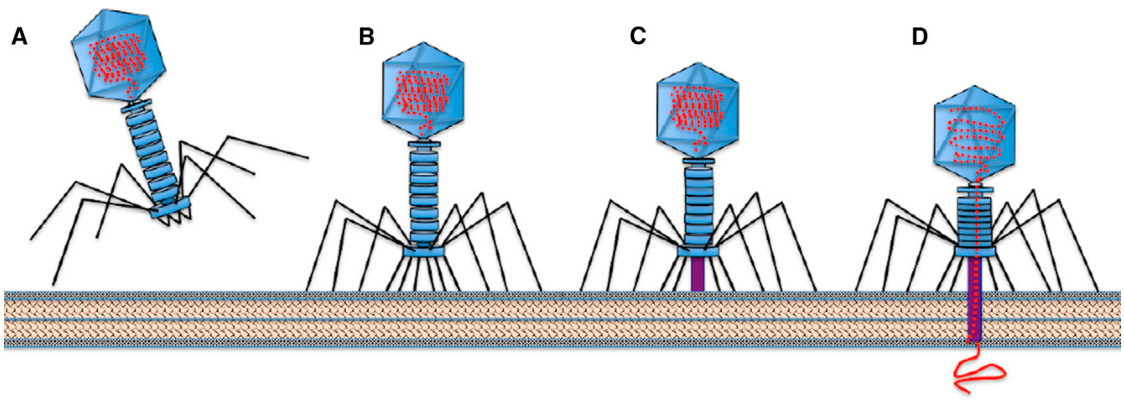

FIGURE 2 Four-stage process for bacteriophage T4 infection: (*A*) bacteriophage T4 recognizes the host cell using the long receptor-binding fibers, (*B*) short fibers bind to the cell surface, (*C*) baseplate undergoes a conformational change that releases the tail tube and signals sheath contraction during which the needlelike tip of tail pierces the cell membrane, and (*D*) interaction of tail tube tip with the *E. coli* cytoplasmic membrane triggers DNA ejection from the capsid into the host cytoplasm. To see this figure in color, go online.

MATERIALS AND METHODS

We open with a summary of our modeling approach to simulate the dynamics of the T4 injection machinery. It is presently impossible to simulate the entire T4 injection machinery at an atomistic level over biologically relevant (e.g., microsecond) timescales using today's computing power. An attractive alternative is to leverage a coarse-grained continuum model of the sheath that can simulate the large (nonlinear) conformational changes over long timescales. To this end, a two-stage modeling process is employed that begins with estimating the elastic properties of the sheath strands using atomistic modeling of a small fraction of the sheath.

Stage 1: Estimating the elastic properties of the sheath strands

As reviewed above, the cylindrical-like tail sheath consists of six interacting helical strands each of which is composed of 23 gp18 subunits that wind around the cylindrical axis of the sheath. When viewed down the cylindrical axis, the gp18 subunits form 23 hexameric rings (1,7). In the extended state, each gp18 subunit interacts with four neighboring subunits: the adjacent two subunits within the strand (intrastrand interaction) and the adjacent two subunits within a ring (interstrand interaction) (6). Cryo-EM maps (6) reveal that, during sheath contraction, the interstrand interactions break whereas the intrastrand interactions remain in retaining the structural integrity of the sheath. The subunits, which are essentially rigid, slide relative to each other during contraction and form new contacts with adjacent subunits. In the fully contracted state, there is a fourfold increase in the number of subunit contacts relative to the extended state, and the number and types of residues involved in all contacts are known; refer to Aksyuk et al. (6) for more details. Despite this wealth of structural information, the elastic properties of the strands are not known, yet they play a central role in powering the dynamic contraction of the sheath. In this first modeling stage, we estimate the elastic bending and torsional stiffness constants for a single strand of the sheath while interacting with its neighboring strands from equilibrium MD simulations. These elastic constants are then incorporated in a continuum model of the entire sheath in the second modeling stage.

Before estimating the elastic stiffness of the sheath strands, the atomic structure of a single ring of six gp18 molecules is obtained for both the extended and contracted sheath conformations from the Protein Data Bank (PDB: 3FOH and 3FOI, respectively) (6). The atomic structure of five adjacent rings (see Fig. 3) follows from using a transformation matrix for rotation and translation obtained from Leiman et al. (1). MD simulations with the NAMD package (18) using the CHARMM 36 all-atom force field (19) are then performed with the resultant structures as input. Langevin dynamics applied on the nonhydrogen atoms with a friction coefficient of 5 ps^{-1} is used to generate the trajectory, and a generalized Born implicit solvent continuum model as implemented in NAMD is used to represent the solvent (18). The system is first slowly heated to an ambient temperature of 298 K, and then equilibrated without any constraints for 5 ns followed by a 20 ns production run. To avoid any overall rotation or translation of the rings during the simulation, the centers of mass of the proteins of the bottom and top rings are constrained using a harmonic potential with a force constant of 10 kcal mol^{-1} $Å^{-2}$.

The twist and curvature of the subunits is equal to the geometrical torsion and curvature of the (instantaneous) helix passing through the mass centers of the subunits. To compute the twist and curvature of the subunits, a best-fit (least-squares) helix is constructed at each integration time step for each helical strand fragment to deduce its (fluctuating) geometric torsion and curvature. The curvature κ_c, and geometric torsion κ_t, are computed from the pitch and radius of the fitted helix during the 20 ns production run for each of the six-strand fragments. The bending stiffness A, and the torsional stiffness C, for each strand are computed from equilibrium fluctuations from the trajectories using the equipartition theorem of classical statistical mechanics as follows:

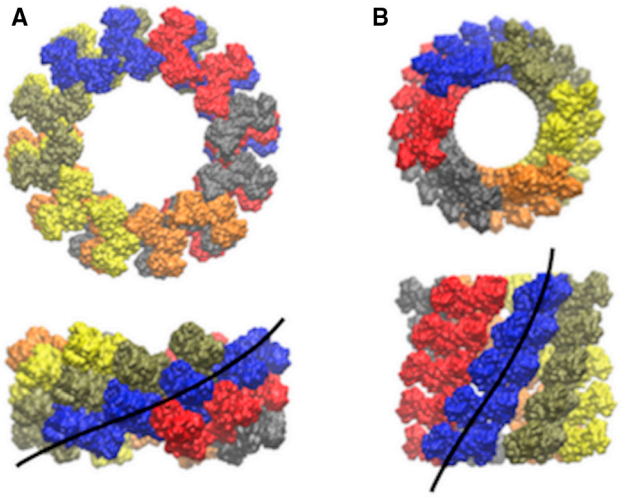

FIGURE 3 Five rings of gp18 subunits that form a fraction of the sheath in the contracted (*A*) and extended (*B*) conformations. Distinct colors denote distinct helical strands. For reference, the black curve denotes the best-fit helix passing through the mass centers of the subunits in one (*blue*) strand. To see this figure in color, go online.

$$\left(\frac{A}{k_B T}\right)^{-1} = \left\langle \left(\kappa_c - \langle \kappa_c \rangle\right)^{tr} \left(\kappa_c - \langle \kappa_c \rangle\right) \right\rangle_{\text{thermal}}, \qquad (1)$$

$$\left(\frac{C}{k_B T}\right)^{-1} = \left\langle \left(\kappa_t - \langle \kappa_t \rangle\right)^{tr} \left(\kappa_t - \langle \kappa_t \rangle\right) \right\rangle_{\text{thermal}}, \qquad (2)$$

where T is the ambient temperature (298 K), k_B is the Boltzmann constant, $\langle\ \rangle$ denotes averaging over time, and $(\ )^{tr}$ stands for transpose.

Stage 2: Modeling the dynamics of the T4 injection machinery

In this second modeling stage, we embed the sheath elastic properties estimated from Stage 1 above in a continuum model of the sheath coupled to a rigid body model for the capsid/neck/tail tube to yield a dynamic model of the entire T4 injection machinery (Fig. 4 *A*). To this end, we build from an approximate single-strand model of the sheath (20) to create a complete shell-like representation of the entire sheath formed by the six interacting helical strands.

Modeling the sheath. The sheath consists of six interacting helical strands of gp18 subunits that connect to the capsid/neck/tail tube at one end and to the baseplate at another end. In our modeling approach, each helical strand is modeled as a homogeneous and isotropic elastic rod as suggested in Fig. 4 *B*. The rationale for constructing a sheath model from six interacting helical rods (strands) follows directly from the experimental evidence that the intrastrand interactions persist throughout the contraction process (7). The assumptions of homogeneity and isotropy are also supported as further described in Appendix A: Homogeneous and Isotropic Rod Assumptions.

The shape of the ith strand (rod) is defined by the 3D centerline curve $R^i(s,t)$ in Fig. 4, where t denotes time, and s is the contour length coordinate measured from the bottom of each strand (where it attaches to the baseplate) to the top of each strand (where it attaches to the neck). At any cross section along the strand we introduce the body-fixed frame $\{a^i_j(s,t)\}$, where the index $j = 1,2,3$ distinguishes three mutually orthogonal unit vectors and the index $i = 1,2,\ldots,6$ distinguishes each of the six strands. Extending an approximation of the sheath having one helical

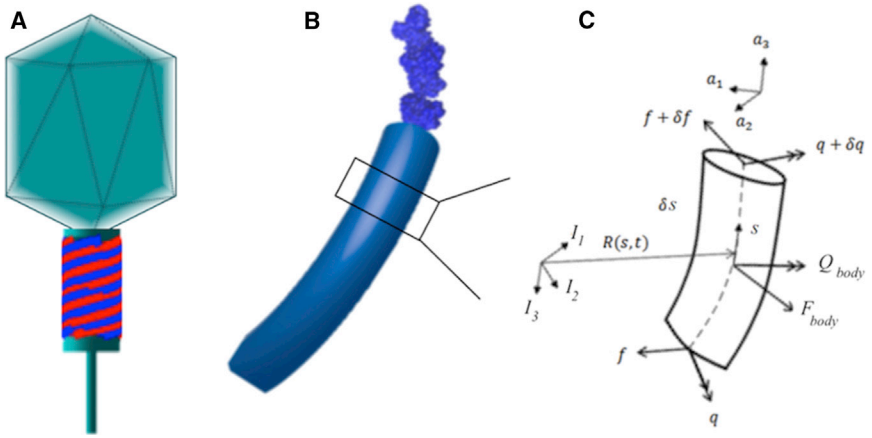

FIGURE 4 (*A*) Dynamic model of the entire T4 injection machinery with the capsid/neck/tail tube assembly represented by a rigid body and the sheath represented by six interacting helical rods (i.e., six interacting helical strands of gp18 subunits). (*B*) Given here is an atomistic model of sheath strand simulated by an elastic rod with the equivalent elastic properties. (*C*) Given here is an infinitesimal element of an elastic (Kirchhoff) rod as a continuum model of a helical strand of gp18. To see this figure in color, go online.

strand (helical rod) (20), we now model all six interacting helical strands (six coupled helical rods) using Kirchhoff rod theory (21). The governing dynamical equations of the *i*th strand (rod) in the body-fixed frame $\{a^i_j\}$ are as follows:

$$\left\{\frac{\partial f}{\partial s}+\kappa\times f=m_s\left(\frac{\partial v}{\partial t}+\omega\times v\right)-F_{\text{body}}\right\}^i, \quad (3)$$

$$\left\{\frac{\partial q}{\partial s}+\kappa\times q=I_s\frac{\partial \omega}{\partial t}+\omega\times I_s\omega+f\times a_3-Q_{\text{body}}\right\}^i, \quad (4)$$

$$\left\{\frac{\partial v}{\partial s}+\kappa\times v=\omega\times a_3\right\}^i, \quad (5)$$

$$\left\{\frac{\partial \omega}{\partial s}+\kappa\times\omega=\frac{\partial \kappa}{\partial t}\right\}^i. \quad (6)$$

Eqs. 3 and 4 describe the balance laws for linear and angular momentum, respectively; and Eqs. 5 and 6 describe constraints on rod inextensibility and rotation, respectively. Therein, $\omega^i(s,t)$ is the angular velocity of the strand cross section, $v^i(s,t)$ is the translational velocity of the strand cross-section centroid, and $\kappa^i(s,t)$ is the strand curvature/twist vector (i.e., the rotation of the body-fixed frame $\{a^i_j\}$ per unit contour length). The quantities $f^i(s,t)$ and $q^i(s,t)$ denote the strand internal force and internal moment, respectively; $m^i{}_s(s)$ is the strand mass/length; and $I^i{}_s(s)$ denotes the (diagonal 3 × 3 tensor) strand principal mass moments of inertia/length. Finally, $a^i{}_3$ is the unit tangent vector at each cross section, and $F^i{}_{\text{body}}(s,t)$ and $Q^i{}_{\text{body}}(s,t)$ denote the sum of all distributed external body forces/length and moments/length, respectively. In particular, $F^i{}_{\text{body}}$ and $Q^i{}_{\text{body}}$ capture the hydrodynamic drag forces and moments on the sheath strands from the surrounding fluid environment as detailed in Appendix B: Hydrodynamic Drag on the Sheath Strands. For further details regarding this rod model formulation, refer to the literature (20,22–24).

In Eq. 4, the internal moment $q^i(s,t)$ is proportional to the curvature/twist vector through the assumption of a linear elastic constitutive law, as follows,

$$q^i(s,t)=B^i\left(\kappa^i-\kappa^i_0\right), \quad (7)$$

where $\kappa^i{}_0$ is the known intrinsic curvature/twist vector of the *i*th helical strand in the stress-free state of the sheath, which is assumed to be the contracted conformation. Here, $B^i(s,t)$ is a diagonal 3 × 3 stiffness tensor, as follows:

$$B^i=\begin{bmatrix}A^i & 0 & 0\\ 0 & A^i & 0\\ 0 & 0 & C^i\end{bmatrix}, \quad (8)$$

for the *i*th strand composed of the bending and torsional stiffness constants estimated from the MD simulations in Stage 1 above. Recall that the MD simulations in Stage 1 consider five rings of the six interacting helical strands. As a result, the reported stiffness properties capture both intrastrand as well as interstrand interactions. In total, Eqs. 3–6 contain four vector unknowns $\{v^i, \omega^i, \kappa^i, f^i\}$ for each of the six interacting strands, yielding a system of 24 nonlinear partial differential equations for solution of the 24 unknowns. This set of equations is discretized in both time and space using the generalized α-method that also employs a shooting method to solve the initial-boundary value problem; refer to the literature (20,22–24) for details on the numerical solution procedure.

Before contraction, the sheath is locked in the extended conformation by noncovalent interactions in a high-energy structure (7). Although the energy stored by the capsid DNA is also large (DNA is packed to near crystalline density), it does not contribute to the forces that penetrate the host cell as the piercing stage (sheath contraction) precedes the DNA ejection phase for *Myoviridae* phages (25) including T4 (1). Even headless (DNA-free) structures such as R2-pyocin and the type VI secretion system employ contracting sheaths to develop the forces for efficiently piercing the cell membrane. The cell membrane-piercing forces derive from the sudden release of the internal energy stored in the extended sheath during contraction. In our model, the internal sheath energy is represented by the strain energy of the six interacting strands as follows:

$$U(t)=\sum_{i=1}^{6}\int_0^1\frac{1}{2}\left(\kappa^i-\kappa^i_0\right)^{tr}B^i\left(\kappa^i-\kappa^i_0\right)ds. \quad (9)$$

Furthermore (and for future reference), the kinetic energy of the entire injection machine is as follows:

$$K(t)=\sum_{i=1}^{6}\int_0^1\frac{1}{2}\left(\omega^{i\,tr}I^i_s\omega^i+v^{i\,tr}m^i_sv^i\right)ds+\frac{1}{2}m_cv_c^2+\frac{1}{2}I_c\omega_c^2, \quad (10)$$

and it is composed of contributions from the six helical strands (sheath) as well as the rigid body translation and rotation of the capsid/neck/tail assembly modeled next. Therein, m_c and I_c are the mass and moment of inertia (about tail tube axis) of the capsid/neck/tail tube assembly, respectively; and v_c and ω_c are the translational velocity and angular velocity of

the capsid/neck/tail tube assembly along and about the tail tube axis, respectively.

Modeling the capsid, neck, tail tube, and baseplate via sheath boundary conditions. In Fig. 1 *A*, the sheath strands attach to the baseplate at the lower end and to the capsid/neck/tail tube assembly at the upper end. Upon contraction, the neck and the baseplate expand radially (7,26), and the locally bound gp18 subunits of the sheath translate outward along and rotate clockwise about the radial axis perpendicular to the tail tube axis (6). Simultaneously, the capsid/neck/tail tube assembly rotates counterclockwise about and translates downward along the tail tube axis. These motions of the gp18 subunits that are bound locally to the baseplate and the neck establish the boundary conditions for the sheath helical strands; further details are provided in Appendix C: The Boundary Conditions on the Sheath Strands. In particular, the upper boundary of a helical strand (bound to the neck) possesses four degrees of freedom: namely, translation along and rotation about the radial axis and translation along and rotation about the tail tube axis. By contrast, the lower boundary of a helical strand (bound to the baseplate) possesses two degrees of freedom: namely, translation along and rotation about the radial axis. The additional translation and rotation about the tail tube axis at the upper end captures the two degree-of-freedom motion of the capsid, neck, and tail tube as they rapidly descend and rotate during the injection process. To this end, the capsid, neck, and tail tube are modeled as a single rigid body bound to the upper end of the six helical strands of the sheath. The resulting two degree-of-freedom equations of motion of this attached rigid body (illustrated in Fig. 4 *A*), which account for the reaction forces and moments from the attached helical strands and the hydrodynamic drag of the surrounding fluid environment, are provided in Appendix C: The Boundary Conditions on the Sheath Strands.

Initial conditions and configuration-dependent helical strand properties. The simulation of the dynamic injection process begins with the sheath at rest in its extended state, which serves as the initial condition for the subsequent numerical integration. The dynamics of the injection is powered by the internal (strain) energy stored in the extended sheath that forms essentially six interacting nonlinear springs (helical strands) driving the rigid capsid/neck/tail tube assembly downward along the tail tube axis, while permitting it to rotate about that axis, per the boundary conditions at the upper end of the strands described above. During this process, the collar and baseplate also undergo known conformational changes that move the upper and lower boundaries of the helical strands radially outward. Similarly, the helical strands increase in length and the elastic constants increase as previously noted above. We model the dynamic changes in any helical strand property $P(t)$ in the simulation by employing the following linear interpolation:

$$P(t) = P_e + (P_c - P_e)\left(\frac{\theta(t)}{345.4^{\circ}}\right), \qquad (11)$$

where $P(t)$ represents any time-varying strand parameter (i.e., radial position of upper and lower strand boundaries, strand radius, strand contour length, strand bending stiffness, strand torsional stiffness) and with P_e and P_c denoting the known values of the parameter in the extended and contracted conformations, respectively. Here $\theta(t)$ denotes the instantaneous rotation of the rigid capsid/neck/tail tube assembly that begins at zero in the extended state, $\theta_e = \theta(0) = 0$ and achieves its maximum value, $\theta_c = 345.4^{\circ}$, in the contracted state. Finally, note that the sixfold symmetry of the sheath structure (7) renders all strand properties identical for the six rods.

RESULTS AND DISCUSSION

Elastic properties of the sheath strands

The MD simulations described above yielded estimates of the averaged bending and torsional stiffness constants of the sheath strands in Table 1. Values are reported for both the extended and contracted sheath conformations together with published values for actin filaments for comparison. Recognizing the sixfold symmetry of the sheath structure (7), the elastic properties calculated for any one strand represents the average for all strands. Because the MD model captures the interactions of five rings of six interacting strands, the reported stiffness constants capture both the interstrand and the intrastrand contributions to the overall sheath stiffness. The estimated bending and torsional stiffness constants of the sheath strands are on the order of those for actin filaments as reported in Gittes et al. (27) and Tsuda et al. (28). Note that the elastic bending and torsional stiffness constants in the contracted conformation are significantly greater than those for the extended conformation. That finding is consistent with the aforementioned cryo-EM data showing a fourfold increase in subunit contacts in the contracted conformation (6). In Fig. 5, the twist and curvature of the best-fit helices (averaged over all six helical strands) are plotted versus time for both the extended and contracted conformations. The amplitudes of the equilibrium fluctuations associated with the extended strands are significantly greater than those for the contracted strands, confirming that the latter are significantly stiffer. Atomistic root mean square deviation (RMSD) fluctuations from the initial structures, calculated for each of the individual six strands, show only small variations of ~2–4 Å from strand to strand; see further details in Appendix D: RMSD of Individual Sheath Strands. Therefore the stiffness values (averaged over all strands) we employ in the dynamic continuum model remain very representative of the values for any strand.

Timescale and pathway of sheath contraction

The bending and torsional stiffness constants from the MD simulations are used as input to the coarse-grain model of the sheath composed of six interacting helical strands where each strand is modeled as a homogenous, isotropic elastic rod but with time-varying (configuration-dependent) elastic constants defined by Eq. 11. The resulting continuum model for the sheath captures the highly nonlinear and rapid dynamic transition from the extended conformation to the

TABLE 1 Elastic Bending and Torsional Stiffness Constants of the Sheath Strands for Phage T4 in Both the Extended and Contracted Conformations

Strand Type	Bending Stiffness (10^{-27} N.m^2)	Torsional Stiffness (10^{-27} N.m^2)
Extended sheath, gp18	26	6.56
Contracted sheath, gp18	35.5	222
Actin filament	73.0 ± 4.38[a]	80.0 ± 1.20[b]

[a]Values for actin filaments from Gittes et al. (27) shown for comparison.
[b]Values for actin filaments from Tsuda et al. (28) shown for comparison.

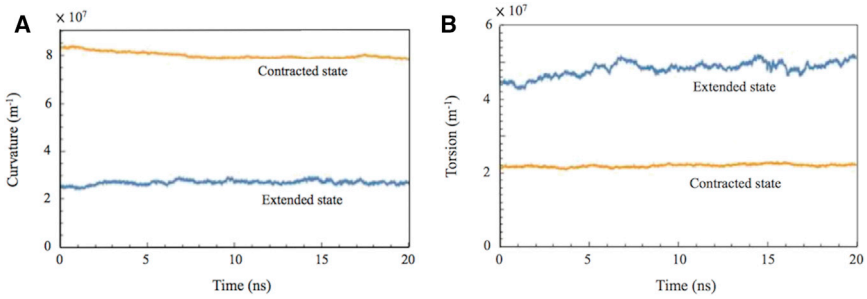

FIGURE 5 Fluctuations of (*A*) the average curvature and (*B*) the average twist for the extended and contracted states during the 20 ns simulation. To see this figure in color, go online.

contracted conformation. The geometrical and material properties of sheath strands and capsid used in the simulation are provided in Appendix E: Geometrical and Material Properties of Bacteriophage T4. Fig. 6 *A* illustrates computed snapshots of the entire T4 injection machinery at 1 μs time increments during the rapid contraction of the sheath during the simulated injection process. Fig. 6 *B* illustrates the associated rotation and translation of the capsid/neck/tail tube assembly as functions of time. This figure reveals that the injection process is estimated to occur on a timescale of several microseconds as mediated by the large drag dominated by the motion of the capsid. This estimated injection time is significantly shorter than that of the subsequent ejection of the viral DNA from the capsid, which is on the order of a minute (~30 s) (29). Note that this model ignores the possible dynamic friction between the tail tube and the sheath as well as friction between the tail tube and the cell membrane during the injection process. These friction forces dissipate energy and also increase the timescale of the injection process relative to the results reported herein.

During injection, the capsid/neck/tail tube assembly rotates counterclockwise approximately one revolution and translates downward ~500 Å consistent with cryo-EM data for the extended and contracted conformations; see, for example, Kostyuchenko et al. (7). The simulation also reveals that the sheath initially undergoes a rapid translation, lasting ~1 μs, which brings the end of the tail tube to the cell surface. After this initial burst of translation is a secondary burst of rotation, lasting ~5 μs, during which the capsid/neck/tail tube assembly completes one revolution. Although the interaction of the host membrane is not considered in this

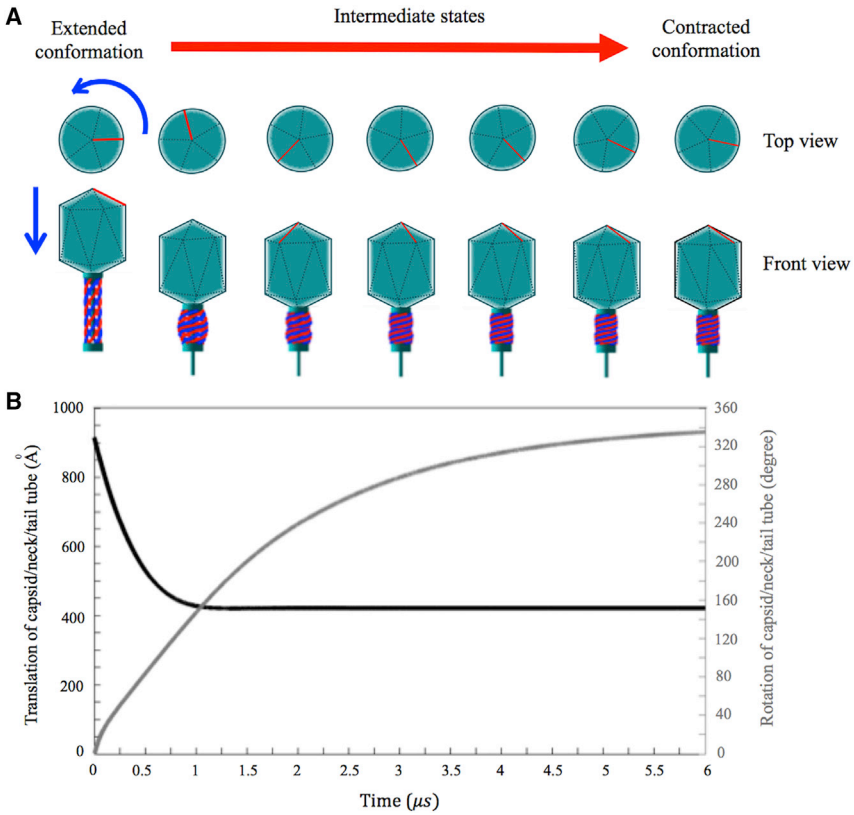

FIGURE 6 Complete model of the T4 injection machinery predicts the dynamic pathway and timescale of the injection process. (*A*) Snapshots of T4 at 1 μs intervals reveal the dynamics of sheath contraction and associated rotation. (*B*) Shown here is the dynamic rotation (*gray curve*) and translation (*black curve*) of the capsid/neck/tail tube assembly. To see this figure in color, go online.

model, it is likely that this two-stage translation and rotation yields the significant force and torque needed to pierce the host membrane. During sheath contraction, all of the strands exhibit the same deformation as they are subject to the identical boundary conditions at the upper end (neck) and the lower end (baseplate). Thus, the sheath also retains sixfold symmetry during this transition. We also note that this model predicts that the sheath develops a slight bulge at the very start of the injection process. Although no experimental evidence yet exists, we believe that this bulge is artificial and likely derives from the approximate treatment of the time-varying strand parameters discussed above. However, this effect remains rather small and it does not influence either the timescale or the pathway illustrated.

Energetics of sheath contraction

The dynamic model of the T4 injection machinery can estimate the energetics of the injection process by employing the expressions for the internal (Eq. 9) and kinetic (Eq. 10) energies. Fig. 7 *A* reports the estimated internal (strain) energy driving the rapid and irreversible injection process. Starting at $t = 0$, the injection process is driven by an estimated 5500 kT sheath internal energy, which is on the order of the experimentally estimated free energy of sheath contraction reported in Arisaka et al. (16). In particular, the free energy of contraction for phage T4 reported in Arisaka et al. (16) is ~5800 kT (3400 kcal/mol gp18) for urea-induced contraction and ~10,000 kT (6000 kcal/mol gp18) for heat-induced contraction. This model ignores possible interactions between the sheath and the tail tube, and considering such sheath-tail tube interactions may further increase the energy of the extended state (as well as possibly introducing dynamic friction between the tail tube and the sheath during contraction). In addition, the maximum force available to rupture the cell membrane is readily computed from Eqs. 3–6 for the extended sheath. This maximum force estimated from this model is 860 pN, which is consistent with the minimum force (lower bound estimate) of 103 pN provided in Falk and James (17).

During contraction, the sheath and capsid are subject to nanoscale hydrodynamic drag forces and moments from the surrounding fluid environment. The drag force/moment pair on the sheath strands is incorporated in the balance laws for linear (Eq. 3) and angular (Eq. 4) momentum through the terms F^{i}_{body} and Q^{i}_{body}, as detailed in Appendix B: Hydrodynamic Drag on the Sheath Strands. The drag force/moment pair on the capsid is captured through the equations of rigid body motion of the capsid/neck/tail tube assembly through the upper boundary conditions on the sheath; refer to Appendix C: The Boundary Conditions on the Sheath Strands. Due to the overwhelmingly large drag at these length scales (30), the kinetic energy of the entire injection machinery remains very small relative to the internal energy as reported in Fig. 7 *A*. Fig. 7 *B* provides a decomposition of the kinetic energy into contributions from the sheath, and the translational and rotational contributions from the capsid/neck/tail tube assembly. The kinetic energy of the capsid/neck/tail tube assembly dominates the kinetic energy of the sheath. This follows from the fact that the mass of the capsid (and genomic DNA)/neck/tail tube assembly (~200 MDa) is ~20 times greater than that of the (six-stranded) sheath (~10 MDa) as estimated from data reported in Leiman et al. (1), Rossmann et al. (2), and Fokine et al. (8).

In Fig. 7 *B*, note the comparable translational and rotational components of the kinetic energy of the capsid/neck/tail tube assembly. However, the translational kinetic energy achieves a maximum well within the first 1 μs of the injection process whereas the maximum of the rotational kinetic energy is delayed. This delay is consistent with the aforementioned predictions of Fig. 6 *B*, which show that the capsid/neck/tail tube assembly undergoes a significant and rapid translation followed by a significant and rapid rotation. This two-punch combination of translation followed by rotation may play a significant role in the efficient piercing of the host membrane by the tip of the tail tube. Consider the advantage of quickly rotating the tip of the tail tube after the tip contacts the host membrane as an efficient mechanism to rupture the membrane.

CONCLUSIONS

This article introduces a dynamic model to simulate, for the first time to our knowledge, the dynamics of the contractile injection machinery of phage T4. The model incorporates the nonlinear dynamics of the sheath from its extended conformation before injection to its contracted conformation after injection as well as the rigid body translation and rotation of

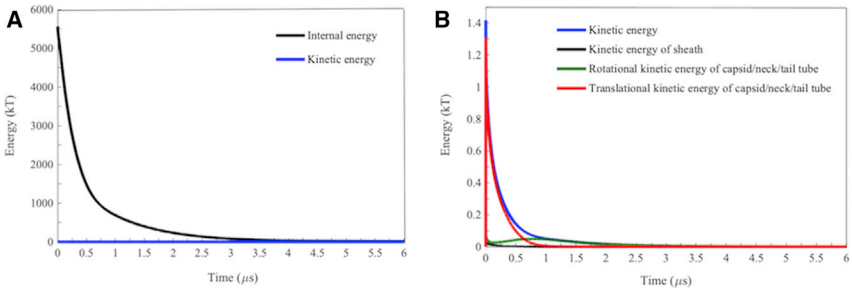

FIGURE 7 Complete model of the T4 injection machinery predicts the energetics of the injection process. (*A*) Internal (strain) and kinetic energies are shown during the injection process as the sheath rapidly collapses from the extended (high energy) conformation to the contracted (low energy) conformation. (*B*) Shown here is the decomposition of kinetic energy into contributions from the sheath and the capsid/DNA/neck/tail tube assembly.

the attached capsid/neck/tail tube domains. As the first step, we estimate the bending and torsional stiffness constants for the helical strands of gp18 that form the elastic sheath from equilibrium MD simulations. Next, we employ the stiffness constants in a continuum model of the elastic sheath composed of six interacting helical strands of gp18 by representing each strand as a homogenous, isotropic elastic rod with time-varying elastic constants. The rigid body motion of the attached capsid/neck/tail tube assembly is captured through a boundary condition for the helical strands and it models the assembly as it translates along and rotates about the tail tube axis. The resulting dynamic model for the entire injection machinery is used to estimate the energetics, timescales, and pathway of the T4 injection process as well as the maximum available force for cell rupture. Simulation results predict that the injection process is powered by ~5500 kT of internal (strain) energy stored in the extended conformation of the sheath, that injection of the tail tube into the host is completed in ~6 μs, and that the extended sheath provides a maximum force of 860 pN to pierce the host. Simulations further reveal that the tail tube motion is essentially a two-stage process that begins with rapid translation along the tail tube axis followed by rapid rotation about that axis. This two-punch combination of translation followed by rotation may be particularly advantageous in piercing of the host membrane by the tip of the tail tube.

The modeling approach can be leveraged in the future to describe the dynamics of other nanoscale injection machines that are powered by contractile sheath structures. Prime examples include the type-VI secretion system, R2 pyocin, and phage ϕ812. Rather remarkably, all of these share the same feature with phage T4 of a contractile sheath structure formed by six interacting helical protein strands.

APPENDIX A: HOMOGENEOUS AND ISOTROPIC ROD ASSUMPTIONS

In this study, each of the six strands of gp18 is modeled as a homogeneous and isotropic elastic rod but with configuration-dependent elastic constants; refer to Table 1. The assumption of homogeneity is quite reasonable based on the uniform contraction theory of the sheath (11) in which all gp18 subunits rotate and translate simultaneously by the same amount. (However, we also recognize a competing theory that assumes that the sheath contraction evolves as a propagating wave (11).) The assumption of isotropy is considered in reference to Fig. 8, which illustrates the MD time-averaged mass density plot of a complete ring of the T4 sheath composed of (a portion of) all six strands. Inspection of Fig. 8 suggests some degree of bending stiffness anisotropy within each strand cross section. However, these differences at the strand level become unimportant when considering the bending of the assembled sheath that is the aggregate of the six coupled strands. Note that the assembled sheath (Fig. 3) is a near-axisymmetric structure (sixfold symmetry) and thus possesses minimal bending anisotropy. In other words, any anisotropy at the strand level averages to isotropic behavior at the sheath level. This isotropic behavior of the sheath can just as well be captured using an isotropic strand model, provided the strand model employs an average bending stiffness constant (for the strand cross section). We estimate this average bending stiffness constant from Eq. 1 for both the extended and the contracted conformations as reported in Table 1.

APPENDIX B: HYDRODYNAMIC DRAG ON THE SHEATH STRANDS

The terms F^i_{body} and Q^i_{body} in Eqs. 3 and 4 denote the hydrodynamic drag force and moment per unit length on the ith sheath strand from the surrounding fluid environment. They are modeled using classical Stoke's regime drag, as follows (30):

$$F^i_{\text{body}} = -\begin{bmatrix} c_{t1} & 0 & 0 \\ 0 & c_{t2} & 0 \\ 0 & 0 & c_{t3} \end{bmatrix} v^i,$$
$$Q^i_{\text{body}} = -\begin{bmatrix} c_{r1} & 0 & 0 \\ 0 & c_{r2} & 0 \\ 0 & 0 & c_{r3} \end{bmatrix} \omega^i, \tag{12}$$

where the drag coefficients are as follows (30):

$$c_{t1} = \frac{4\pi\eta}{ln\left(\frac{L}{2R_s}\right) + 0.84}, \quad c_{t2} = c_{t1}, \quad c_{t3} = \frac{2\pi\eta}{ln\left(\frac{L}{2R_s}\right) - 0.2},$$
$$c_{r1} = \frac{\frac{1}{3}\pi\eta L^2}{ln\left(\frac{L}{2R_s}\right) - 0.66}, \quad c_{r2} = c_{r1}, \quad c_{r3} = 4\pi\eta R_s^2. \tag{13}$$

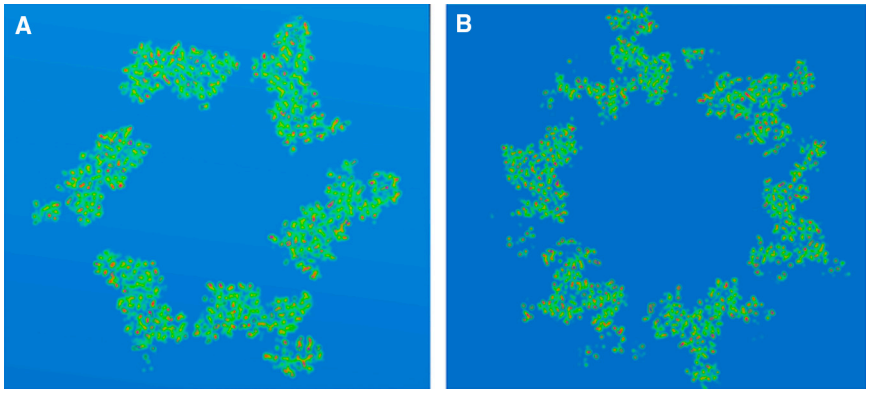

FIGURE 8 Schematic of the time-averaged mass density for the cross section of a single ring of the T4 sheath in (*A*) the extended state and (*B*) the contracted state. To see this figure in color, go online.

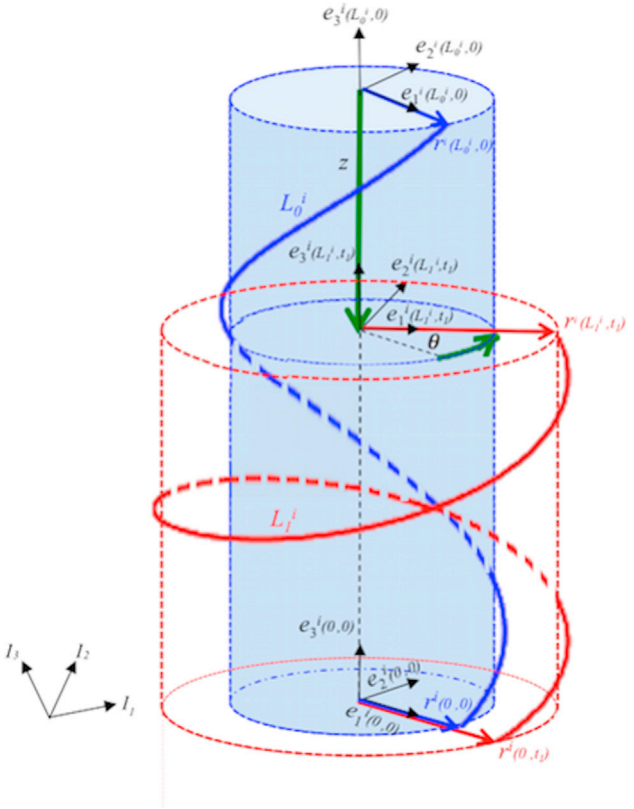

FIGURE 9 Schematic of a single strand in the extended conformation at $t = 0$ (*blue helix*) and in an intermediate state at $t = t_1$ (*red helix*). Frame $\{e^i_j(s,t)\}$denotes a cylindrical frame having radial, circumferential, and vertical unit directions (e_1, e_2, e_3), which may vary with contour length s and time t. At the lower boundary, the cylindrical frame remains constant and is denoted $\{e^i_j(0,0)\}$; at the upper boundary, the cylindrical frame varies with time and with time-varying contour length and is denoted $\{e^i_j(L^i(t),t)\}$. Also illustrated are the radius of the baseplate $r^i(0,t)$, the radius of the neck $r^i(L^i(t),t)$, and the strand contour length in the extended conformation L^i_0 and in the intermediate state L^i_1. Finally, z and θ denote the translation and rotation of the capsid/neck/tail tube assembly along and about the tail tube axis (e_3), respectively. To see this figure in color, go online.

Here, $R_s = R_s(t)$ and $L = L(t)$ denote the radius and contour length of each strand (rod), respectively, at time t updated from Eq. 11, and η is the viscosity of water.

APPENDIX C: THE BOUNDARY CONDITIONS ON THE SHEATH STRANDS

The boundary conditions on the sheath strands impose constraints on the velocity, angular velocity, and internal force/moments at each end of the strand. Relative to the cylindrical frame $\{e^i_j(s,t)\}$ shown in Fig. 9, the boundary conditions at the lower end ($s = 0$) are as follows:

$$v^i_{e1}(0,t) = v_r(t), \quad v^i_{e2}(0,t) = 0, \quad v^i_{e3}(0,t) = 0, \tag{14a}$$

$$q^i_{e1}(0,t) = 0, \quad \omega^i_{e2}(0,t) = 0, \quad \omega^i_{e3}(0,t) = 0, \quad i = 1,2,..,6. \tag{14b}$$

These conditions describe the facts that, at the lower end, 1) the radial velocity component is prescribed (by the time-varying radius of the neck per Eq. 11), whereas the velocity components in the two orthogonal direction vanish (Eq. 14a); and 2) the strand cross section is free to rotate about the radial direction, but rotations about the two orthogonal directions vanish (Eq. 14b). The index $i = 1,2,\ldots,6$ denotes each of the six helical strands.

At the upper end ($s = L(t)$), the boundary conditions are as follows:

$$v^i_{e1}(L,t) = v_r(t), \quad v^i_{e2}(L,t) = r^i_{e1}(L,t)\omega^i_{e3}(L,t), \quad \omega^i_{e2}(L,t) = 0, \quad q^i_{e1}(L,t) = 0, \tag{15a}$$

$$\sum_{i=1}^{6} f^i_{e3}(L,t) + F_{\text{drag}}(t) = m_c \frac{\partial v_c(t)}{\partial t}, \tag{15b}$$

$$\sum_{i=1}^{6} q^i_{e3}(L,t) + \sum_{i=1}^{6} \left[r^i(L,t) \times f^i(L,t)\right]_{e3} + Q_{\text{drag}}(t) = I_c \frac{\partial \omega_c(t)}{\partial t}. \tag{15c}$$

These conditions describe the facts that, at the upper end, 1) the radial velocity component is prescribed by the time-varying radius of the neck per Eq. 11, whereas the velocity component in the circumferential direction is determined by the rotation rate of the capsid/neck/tail tube assembly about the tail tube axis from Eq. 15a; and 2) the angular rate about the circumferential direction vanishes whereas the strand cross section is free to rotate about the radial direction, taken from Eq. 15b. In addition, Eq. 15c gives the balance laws of linear and angular momentum governing the rigid body motion of the attached capsid/neck/tail tube assembly, which translates along the tail tube axis with velocity $v_c(t) = v^i_{e3}(L(t),t)$ and rotates about this axis with

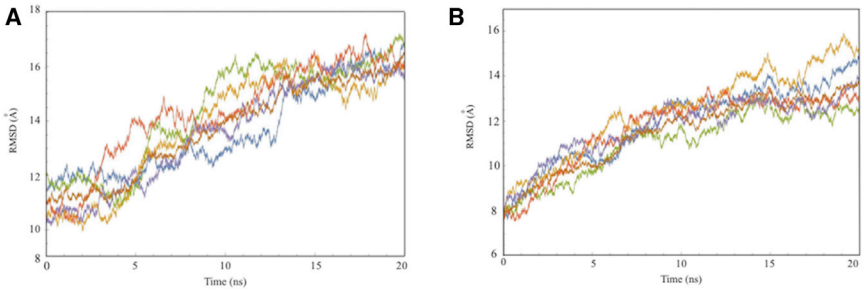

FIGURE 10 Atomistic RMSDs from the initial unequilibrated structure for each of the six individual helical strands for the extended (*A*) and contracted (*B*) states during the 20 ns production run. Different colors denote different strands. To see this figure in color, go online.

TABLE 2 Geometrical and Material Properties of Bacteriophage T4 Used in the Dynamic Model of Sheath Contraction

Geometrical/Material Properties	Contracted State (Reference)	Extended State (Reference)
Bending stiffness of sheath strand, A (10^{-27} N.m^2)	35.5	26
Torsional stiffness of sheath strand, C (10^{-27} N.m^2)	222	6.56
Mass density of subunit gp18, ρ (kg/m^3)	1130	1130
Mass of each subunit gp18 (kDa)	71.2 (2)	71.2
Mass of capsid/DNA/neck/tail tube, m_c (MDa)	1.971 (1,2,8)	1.971
Arc length of sheath strand, L (Å)	1483.5	1079.8
Radius of helix passing through each strand, r (Å)	112.66	84.45
Height of sheath, H (Å)	420 (7)	925 (7)
Radius of rod (sheath strand), R_s (Å)	22.72	26.64
Number of sheath strand turns, n	2.01 (7)	1.05 (7)
Height of capsid, l (Å)	1195 (8)	1195
Radius of capsid, R_c (Å)	430 (8)	430

angular velocity $\omega_c(t) = \omega^i_{e3}(L(t),t)$. Fig. 9 illustrates the cylindrical frames $\{e^i_j(s,t)\}$ at the upper and lower boundaries as well as the time-varying radius of the baseplate $r^i(0,t)$ and neck $r^i(L^i(t),t)$. The motion of the capsid/neck/tail tube assembly (Eq. 15c) is substantially influenced by the hydrodynamic drag force and moment from the surrounding fluid environment, which can be approximated by the following (30):

$$F_{\text{drag}} = -C_t v_c, \quad C_t = \frac{2\pi\eta l}{ln\left(\frac{l}{2R_c}\right) - 0.2}, \qquad Q_{\text{drag}} = -C_r \omega_c, \quad C_t = 4\eta\pi l R_c^2, \tag{16}$$

where C_t and C_r are the force and moment drag coefficients, respectively. Here, l is the length and R_c is the radius of the (assumed) cylindrical capsid/neck/tail tube assembly, which possesses mass m_c and moment of inertia I_c. Finally, the quantities $f^i_{e3}(L,t)$ and $q^i_{e3}(L,t)$ appearing in Eq. 15c are the reaction force and moment components of i th strand, respectively, at the neck along the e_3 direction.

APPENDIX D: RMSD OF INDIVIDUAL SHEATH STRANDS

Fig. 10 provides the atomistic RMSD for each of the six helical strands in both extended and contracted states.

APPENDIX E: GEOMETRICAL AND MATERIAL PROPERTIES OF BACTERIOPHAGE T4

Table 2 provides a summary of the geometrical and material parameters for the dynamical model of T4.

AUTHOR CONTRIBUTIONS

A.M. created the continuum model and the results therefrom and drafted the manuscript. A.C. created the atomistic model and results therefrom. I.A. and N.C.P. advised the investigators and edited the manuscript.

ACKNOWLEDGMENTS

This material is based upon work supported by the National Science Foundation (NSF) under grant No. CMMI-1404747.

REFERENCES

1. Leiman, P. G., P. R. Chipman, …, M. G. Rossmann. 2004. Three-dimensional rearrangement of proteins in the tail of bacteriophage T4 on infection of its host. *Cell.* 118:419–429.
2. Rossmann, M. G., V. V. Mesyanzhinov, …, P. G. Leiman. 2004. The bacteriophage T4 DNA injection machine. *Curr. Opin. Struct. Biol.* 14:171–180.
3. Leiman, P. G., V. A. Kostyuchenko, …, M. G. Rossmann. 2000. Structure of bacteriophage T4 gene product 11, the interface between the baseplate and short tail fibers. *J. Mol. Biol.* 301:975–985.
4. Kanamaru, S., P. G. Leiman, …, M. G. Rossmann. 2002. Structure of the cell-puncturing device of bacteriophage T4. *Nature.* 415:553–557.
5. Yap, M. L., T. Klose, …, M. G. Rossmann. 2016. Role of bacteriophage T4 baseplate in regulating assembly and infection. *Proc. Natl. Acad. Sci. USA.* 113:2654–2659.
6. Aksyuk, A. A., P. G. Leiman, …, M. G. Rossmann. 2009. The tail sheath structure of bacteriophage T4: a molecular machine for infecting bacteria. *EMBO J.* 28:821–829.
7. Kostyuchenko, V. A., P. R. Chipman, …, M. G. Rossmann. 2005. The tail structure of bacteriophage T4 and its mechanism of contraction. *Nat. Struct. Mol. Biol.* 12:810–813.
8. Fokine, A., P. R. Chipman, …, M. G. Rossmann. 2004. Molecular architecture of the prolate head of bacteriophage T4. *Proc. Natl. Acad. Sci. USA.* 101:6003–6008.
9. Kostyuchenko, V. A., P. G. Leiman, …, M. G. Rossmann. 2003. Three-dimensional structure of bacteriophage T4 baseplate. *Nat. Struct. Biol.* 10:688–693.
10. Moody, M. F. 1967. Structure of the sheath of bacteriophage T4: I. Structure of the contracted sheath and polysheath. *J. Mol. Boil.* 25:167–200.
11. Moody, M. F. 1973. Sheath of bacteriophage T4. III. Contraction mechanism deduced from partially contracted sheaths. *J. Mol. Biol.* 80:613–635.
12. Taylor, N. M., N. S. Prokhorov, …, P. G. Leiman. 2016. Structure of the T4 baseplate and its function in triggering sheath contraction. *Nature.* 533:346–352.
13. Matsuzaki, S., M. Rashel, …, S. Imai. 2005. Bacteriophage therapy: a revitalized therapy against bacterial infectious diseases. *J. Infect. Chemother.* 11:211–219.
14. Sulakvelidze, A., Z. Alavidze, and J. G. Morris, Jr. 2001. Bacteriophage therapy. *Antimicrob. Agents Chemother.* 45:649–659.
15. Petrenko, V. A., and V. J. Vodyanoy. 2003. Phage display for detection of biological threat agents. *J. Microbiol. Methods.* 53:253–262.
16. Arisaka, F., J. Engel, and H. Klump. 1981. Contraction and dissociation of the bacteriophage T4 tail sheath induced by heat and urea. *Prog. Clin. Biol. Res.* 64:365–379.
17. Falk, W., and R. D. James. 2006. Elasticity theory for self-assembled protein lattices with application to the martensitic phase transition in bacteriophage T4 tail sheath. *Phys. Rev. E Stat. Nonlin. Soft Matter Phys.* 73:011917.

18. Phillips, J. C., R. Braun, …, K. Schulten. 2005. Scalable molecular dynamics with NAMD. *J. Comput. Chem.* 26:1781–1802.

19. Brooks, B. R., R. E. Bruccoleri, …, M. Karplus. 1983. Charmm: a program for macromolecular energy, minimization, and dynamics calculations. *J. Comput. Chem.* 4:187–217.

20. Maghsoodi, A., A. Chatterjee, …, N. C. Perkins. 2016. A first model of the dynamics of the bacteriophage T4 injection machinery. *J. Comput. Nonlinear Dyn.* 11:041026.

21. Love, A. E. H. 2013. A Treatise on the Mathematical Theory of Elasticity. Cambridge University Press, Cambridge, UK.

22. Goyal, S., T. Lillian, …, N. C. Perkins. 2007. Intrinsic curvature of DNA influences LacR-mediated looping. *Biophys. J.* 93:4342–4359.

23. Hirsh, A. D., T. D. Lillian, …, N. C. Perkins. 2013. A model for highly strained DNA compressed inside a protein cavity. *J. Comput. Nonlinear Dyn.* 8:031001.

24. Hirsh, A. D., and N. C. Perkins. 2015. DNA buckling in bacteriophage cavities as a mechanism to aid virus assembly. *J. Struct. Biol.* 189:251–258.

25. Rossmann, M. G., and V. B. Rao. 2011. Viral Molecular Machines, Vol. 726. Springer Science & Business Media, Berlin, Germany.

26. Fokine, A., Z. Zhang, …, M. G. Rossmann. 2013. The molecular architecture of the bacteriophage T4 neck. *J. Mol. Biol.* 425:1731–1744.

27. Gittes, F., B. Mickey, …, J. Howard. 1993. Flexural rigidity of microtubules and actin filaments measured from thermal fluctuations in shape. *J. Cell Biol.* 120:923–934.

28. Tsuda, Y., H. Yasutake, …, T. Yanagida. 1996. Torsional rigidity of single actin filaments and actin-actin bond breaking force under torsion measured directly by in vitro micromanipulation. *Proc. Natl. Acad. Sci. USA.* 93:12937–12942.

29. Letellier, L., P. Boulanger, …, P. Jacquot. 2003. Channeling phage DNA through membranes: from in vivo to in vitro. *Res. Microbiol.* 154:283–287.

30. Howard, J. 2001. Mechanics of Motor Proteins and the Cytoskeleton. Sinauer Associates, Sunderland, MA.